Low-energy electronic excitations and band-gap renormalization in CuO

Claudia Rödl,[1,2,3] Kari O. Ruotsalainen,[4,5] Francesco Sottile,[1,3] Ari-Pekka Honkanen,[4] James M. Ablett,[5] Jean-Pascal Rueff,[5,6] Fausto Sirotti,[5] Roberto Verbeni,[7] Ali Al-Zein,[7,8] Lucia Reining,[1,3] and Simo Huotari[4]

[1]*Laboratoire des Solides Irradiés, École polytechnique, CNRS, CEA, Université Paris-Saclay, 91128 Palaiseau cedex, France*

[2]*Institut für Festkörpertheorie und -optik, Friedrich-Schiller-Universität, Max-Wien-Platz 1, 07743 Jena, Germany*

[3]*European Theoretical Spectroscopy Facility (ETSF)*

[4]*Department of Physics, University of Helsinki, PO Box 64, FI-00014 Helsinki, Finland*

[5]*Synchrotron SOLEIL, l'Orme des Merisiers, Saint-Aubin, 91192 Gif-sur-Yvette cedex, France*

[6]*Laboratoire de Chimie Physique – Matière et Rayonnement, Université Pierre et Marie Curie and CNRS UMR 7614, 75231 Paris cedex 05, France*

[7]*ESRF – The European Synchrotron, CS40220, 38043 Grenoble cedex 9, France*

[8]*Physics Department, Faculty of Science, Beirut Arab University (BAU), Beirut, Lebanon*

(Received 9 September 2016; revised manuscript received 7 March 2017; published 18 May 2017)

Combining nonresonant inelastic x-ray scattering experiments with state-of-the-art *ab initio* many-body calculations, we investigate the electronic screening mechanisms in strongly correlated CuO in a large range of energy and momentum transfers. The excellent agreement between theory and experiment, including the low-energy charge excitations, allows us to use the calculated dynamical screening as a safe building block for many-body perturbation theory and to elucidate the crucial role played by *d*-*d* excitations in renormalizing the band gap of CuO. In this way we can dissect the contributions of different excitations to the electronic self-energy which is illuminating concerning both the general theory and this prototypical material.

DOI: 10.1103/PhysRevB.95.195142

I. INTRODUCTION

Understanding electron excitation spectra of correlated materials is a major challenge for condensed-matter physics. The simplest approach to describe excitation spectra is in terms of transitions between independent-particle states, but such a naive picture is almost never valid. In *sp* semiconductors, such as Si, many spectral features can be captured using the concept of effective particles in a mean field or quasiparticles (QP), which are weakly interacting effective particles with a relatively long lifetime. In so-called strongly correlated materials, for instance transition-metal oxides (TMOs), even the QP picture may break down. Often, the term "strong correlation" is associated with the presence of low-energy excitations that lead to a substantial transfer of spectral weight from the QPs to satellites. The resulting spectra are qualitatively different from any independent-particle spectrum [1].

In the excitation spectrum, the fundamental band gap is a key quantity with particular theoretical and practical interest. In *strongly correlated* Mott insulators [2], the QPs at the Fermi level vanish and a gap is formed between Hubbard bands [3] to which the QP spectral weight is transferred. The description of this phenomenon requires highly advanced theoretical approaches, e.g., dynamical mean-field theory (DMFT) [4], which in practical calculations often rely on models. In *weakly correlated* systems with a QP gap, such as *sp* semiconductors, already the Hartree-Fock approximation yields a band gap, even though it is in general far too large: The Hartree-Fock gap lacks renormalization by screening. The screening in weakly correlated materials is dominated by the excitation of plasmons, which are typically found at energies around 20 eV and can be well described by single-plasmon-pole models [5]. *Real correlated* materials are often situated between these two extremes. Their understanding requires more detailed quantitative investigations.

Here we tackle the band-gap problem in cupric oxide (CuO), a prototypical strongly correlated oxide. CuO exhibits a rich excitation spectrum with low-energy electronic excitations that are usually associated with strongly correlated materials. In particular, the low-energy physics gives rise to phenomena like antiferromagnetism with two different Néel temperatures [6] and multiferroicity [7] reflecting the presence of competing equilibrium phases that are close in energy. Moreover, CuO constitutes the parent compound of the cuprate high-temperature superconductors [8]. Its electronic structure is governed by the open Cu 3*d* shell which strongly hybridizes with the O 2*p* states yielding a system with pronounced many-body character. Structural and electronic properties of CuO have been studied using density-functional theory (DFT) with local or orbital-dependent functionals [9]. Model Hamiltonians have been employed to investigate the electronic structure, in particular in the context of superconductivity [10]. However, whereas cuprates have been studied extensively using methods for strong correlation such as DMFT (see, for instance, Refs. [11,12]), these approaches have not been applied to CuO itself.

The band gaps of other TMOs, such as MnO, FeO, CoO, and NiO, are understood and have been calculated [13] with good accuracy using many-body perturbation theory, but CuO is the black sheep of this family and has escaped any *ab initio* theory [14,15] so far. Our combined state-of-the-art experimental and *ab initio* many-body perturbation theory (MBPT) study aims to elucidate the mechanisms that determine the band gap of CuO and explains them by means of a coupling of electronic and low-energy charge excitations.

In MBPT, the electronic self-energy Σ, which *exactly* describes the electron interaction including *all* correlation effects, can be written as $\Sigma = iGW\Gamma$, where G is the one-particle Green's function, W is the dynamically screened Coulomb interaction, and the vertex Γ is a functional of G and

W. The central quantity of this formulation is $W = \varepsilon^{-1}v$, with v as the bare Coulomb interaction and $\varepsilon^{-1}(\mathbf{q},\omega)$ as the exact, measurable, momentum-, and frequency-dependent inverse dielectric function. This way of representing Σ implicitly supposes that the dominating physics is the coupling of electrons or holes (which are contained in G) with electron-hole excitations (contained in W), e.g., excitons or plasmons. The vertex Γ is treated as a correction; $\Gamma = 1$ yields the widely used GW approximation (GWA) [16]. In strongly correlated materials, however, Γ might be very different from 1. Whether or not Γ is important is in principle easy to detect by comparing GW results to experiment. However, this supposes that the exact W is known. For the interpretation of electronic spectra of CuO, the *first key question* to be answered is therefore: To which extent can we describe and understand screening in CuO? Combining inelastic x-ray scattering (IXS) and electron-energy loss spectroscopy (EELS) experiments with *ab initio* calculations allows us to directly verify this point.

Hence we can tackle the *second important question*: Is the coupling of electrons and holes with electron-hole excitations, which is the physics contained in the GWA, sufficient to describe the QP excitations in CuO and explain its band gap? Indeed, this question has remained open, although, recently, the electronic structure of CuO has been calculated within the GWA [14,15]. The problem is that the band gap of CuO is strikingly sensitive to different approximations for W. The most sophisticated QP self-consistent GW scheme [13], which iterates W to self-consistency including QP corrections, yields a direct band gap of 4.2 eV [15], i.e., an overestimation by 250% of the experimental zero-temperature band gap of 1.67 eV [17]. Here we provide an explanation for this pathologic behavior.

In Sec. II we outline the details of the employed experimental and computational methods. In Sec. III we compare our experimental and calculated loss spectra of CuO. Based on the agreement between RPA loss spectra and the experimental data, we investigate the impact of the low-energy excitations in the loss function on the band-gap renormalization in Sec. IV. Finally, Sec. V summarizes our work and puts it into context with recent advances and open questions concerning the many-body body physics of strongly correlated systems.

II. EXPERIMENTAL AND COMPUTATIONAL DETAILS

A. IXS and EELS

Room-temperature nonresonant IXS spectra were recorded on a CuO single crystal at the beamline ID20 of the European Synchrotron Radiation Facility (ESRF). The incident radiation was monochromatized with a Si(111) crystal and focused onto the sample with Kirkpatrick-Baez mirrors. The scattered radiation was analyzed with a diced Si(553) analyzer in the Johann geometry with a 2 m Rowland circle radius. The total energy resolution of the setup was 1 eV, as measured from the elastic line. The spectra were recorded by scanning the incident energy ($\sim$8.8 keV) and keeping the analyzer Bragg angle fixed. The scattering vectors were aligned with the reciprocal lattice vectors [100] and [110] (of the chemical conventional unit cell) using x-ray diffraction. The backgrounds were removed by fitting Pearson VII functions to the energy-loss side tails of the elastic lines. Experimental spectra were normalized with respect to the theoretical spectra by applying the f-sum rule in an energy range between 8 and 50 eV.

Complementary room-temperature EELS spectra were recorded at the UHV experimental station of the TEMPO beamline [18] at SOLEIL. An electron beam with 1450 eV kinetic energy and an energy resolution of about 280 meV impinged on the sample surface with an angle of 50°. EELS spectra were measured at normal emission with a Scienta SES 2002 electron-energy analyzer. The experimental setup follows Ref. [19].

B. Many-body calculations

We calculated the electronic structure, the loss function, and the electronic self-energy using DFT and MBPT as implemented in VASP [20,21], with the projector-augmented wave method and a plane-wave cutoff of 450 eV. In these simulations, the experimental lattice parameters [22] and the experimentally observed ground-state magnetic ordering [6] were employed for the 16-atom monoclinic unit cell [23].

Exchange and correlation in the DFT Kohn-Sham Hamiltonian were described by the PBE density functional [24] with an additional on-site interaction $U = 4$ eV for the Cu $3d$ states. The value of U is *not* chosen to reproduce the band gap, but results from matching the DFT+U valence-band density of states with the one from a hybrid-functional calculation (see Ref. [15]). This procedure ensures in particular that the binding energy of the Cu $3d$ states with respect to the O $2p$ states and, hence, the hybridization between these two groups of states is well described. GW quasiparticle corrections were calculated on a $2 \times 3 \times 2$ $\mathbf{k}$-point grid within the QP self-consistent GW scheme, but keeping the screened Coulomb interaction W fixed throughout the iteration (scGW_0) [15,21]. Electronic states in the self-energy were summed over 384 bands. In a final step, the GW self-energy was evaluated on top of the converged QP electronic structure on a grid of 255 frequency points.

We evaluated the momentum- and frequency-dependent loss function $-\operatorname{Im}\varepsilon^{-1}(\mathbf{q},\omega)$ including crystal local-field effects both in the random-phase approximation (RPA) and by solving the Bethe-Salpeter equation (BSE) [25]. In the RPA, the loss function $-\operatorname{Im}\varepsilon^{-1}(\mathbf{q},\omega)$ was calculated from the PBE+U electronic structure using 384 bands, a $3 \times 6 \times 3$ $\mathbf{k}$-point mesh, and 200 frequency grid points. Local-field effects up to a cutoff energy of 200 eV have been taken into account in the inversion of the dielectric matrix $\varepsilon_{\mathbf{GG'}}(\mathbf{q}_{\mathrm{red}},\omega)$ where $\mathbf{q} = \mathbf{q}_{\mathrm{red}} + \mathbf{G}$ is split into a reduced vector in the first Brillouin zone and a reciprocal lattice vector. The frequency-dependent lifetime broadening of the loss spectra was obtained from the GW QP lifetimes of electron and hole. The BSE was solved for vanishing momentum transfer $\mathbf{q} \to 0$ to calculate the loss function including excitonic and local-field effects. The electron-hole-pair Hamiltonian with the matrix elements of the bare and screened Coulomb interaction was constructed from the GW quasiparticle electronic states. Independent electron-hole-pair transitions on a grid of $2 \times 3 \times 2$ $\mathbf{k}$ points up to a cutoff energy of 18 eV have been taken into account. The dielectric function was calculated from the

excitonic eigenstates obtained by direct diagonalization of the Hamiltonian.

III. LOSS FUNCTION

We first focus on the dynamical screening properties of CuO: On the experimental side, IXS offers a view on the dynamic structure factor (DSF) $S(\mathbf{q},\omega) = -\operatorname{Im}\varepsilon^{-1}(\mathbf{q},\omega)/[\pi v(\mathbf{q})]$ and, hence, on the loss function $-\operatorname{Im}\varepsilon^{-1}(\mathbf{q},\omega)$ for a wide range of momentum transfers $\mathbf{q}$. Complementary to IXS, EELS is an appropriate technique to access the loss function for small $\mathbf{q}$. Up to now, only the d-d excitations at low energies have been studied experimentally by resonant [26] and nonresonant IXS [27] at large $\mathbf{q}$, and low-resolution $\mathbf{q}$-integrating EELS experiments have been performed [28]. For the theoretical calculation of the overall $S(\mathbf{q},\omega)$, it is not even well understood which method is appropriate. The standard approach to describe IXS is the RPA where plasmonlike structures are well described as superpositions of electron-hole pairs without any electron-hole attraction and where the electron and the hole are approximated in some mean-field independent-particle picture. In correlated materials like CuO, however, one might expect that such a simple picture breaks down.

A. Loss function for finite momentum transfers

Figure 1 compares the measured and calculated DSF of CuO for a wide range of frequencies and momentum transfers along the [110] and [100] directions. The sum of the QP lifetimes of electron and hole, as obtained from the imaginary part of the self-energy at the QP energy, is included in the theoretical spectra and a further Gaussian broadening of 1.0 eV has been applied. The lowest measured momentum transfers correspond to $\mathbf{q} = [\frac{1}{3}\frac{1}{3}0]$ ($|\mathbf{q}| = 0.76$ Å^{-1}) and $\mathbf{q} = [\frac{1}{3}00]$ ($|\mathbf{q}| = 0.45$ Å^{-1}). The RPA spectra agree very well with the experimental data for $\mathbf{q}$ up to $\sim$3 Å^{-1}.

The good agreement for small $\mathbf{q}$ is not a coincidence: Fig. 2(a) displays the loss function $-\operatorname{Im}\varepsilon^{-1}(\mathbf{q}\to 0,\omega)$ calculated within three approaches: (i) in the RPA, (ii) in the RPA with added QP corrections (QP-RPA), and (iii) taking also the electron-hole attraction, i.e., excitonic effects, into account (BSE). The BSE spectrum is very close to the original RPA result and its structure is confirmed by EELS measurements integrated over small $\mathbf{q}$. QP corrections and the electron-hole attraction cancel to a large extent: Adding merely QP corrections blueshifts the spectrum by $\sim$1 eV, while the inclusion of excitonic effects (BSE) recovers the RPA peak energies. For small $\mathbf{q}$, this cancellation has been discussed for long-range plasmons (e.g., in Si [29]) as well as for localized excitations (e.g., in V_2O_3 [30]). The low-energy IXS peaks at high $\mathbf{q}$ are not well described within the RPA. This is interesting and deserves further investigation. However, it goes beyond the scope of our work, since the high-$\mathbf{q}$ excitations are of little relevance for the band-gap renormalization, as we will argue below.

Our MBPT calculations unravel the nature of the excitations in the loss function: The lowest-energy optical excitations in CuO [i.e., peaks in $\operatorname{Im}\varepsilon(\mathbf{q}\to 0,\omega)$] are due to transitions from the highest valence states with mixed Cu $3d_{x^2-y^2}$ and

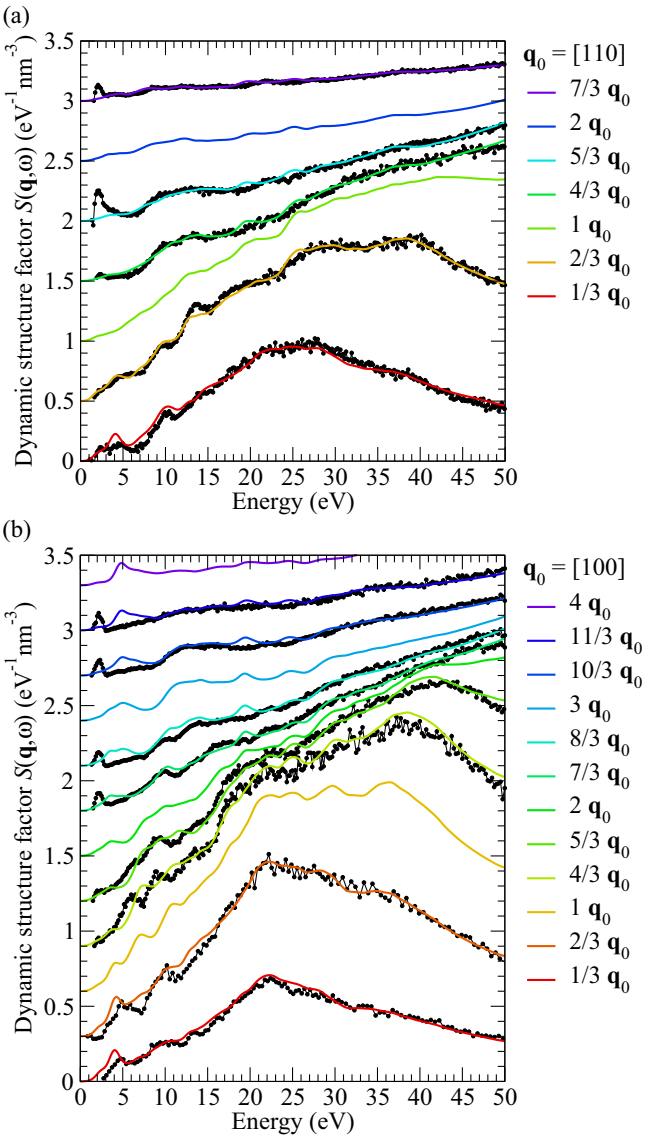

FIG. 1. Dynamic structure factor $S(\mathbf{q},\omega)$ for momentum transfers $\mathbf{q}$ along the [110] (a) and [100] (b) directions of the conventional chemical unit cell. Experimental data from IXS (dots) are compared to calculated spectra in the RPA (lines). For better visibility, the spectra for different $\mathbf{q}$ are offset vertically.

O $2p$ character to the empty Cu $3d_{x^2-y^2}$ states [see Figs. 2(b) and 2(c)]. The second absorption peak stems from O $2p$ to Cu $3d_{x^2-y^2}$ transitions. These excitations go along with zeros of $\operatorname{Re}\varepsilon(\mathbf{q}\to 0,\omega)$ indicating collective charge fluctuations which result in the shoulder S and the peak A in the loss spectrum [see Fig. 2(a)]. Peak B is a collective excitation reflected by the linear increase of $\operatorname{Re}\varepsilon(\omega)$ and the linear decrease of $\operatorname{Im}\varepsilon(\omega)$ which has been seen also in other TMOs [31]. The broad structure P (that peaks at 22–23 eV for $\mathbf{q}\to 0$, disperses quadratically, and flattens for higher $\mathbf{q}$) is the main plasmon. Its lower edge at 19 eV can be identified with the onset of plasma excitations of the O $2p$ valence electrons (for which the classical plasma frequency is 20.2 eV) and the associated Fano resonance [32]. This peak occurs at similar energies in other TMOs [33]. The low-energy structures S and A disperse only

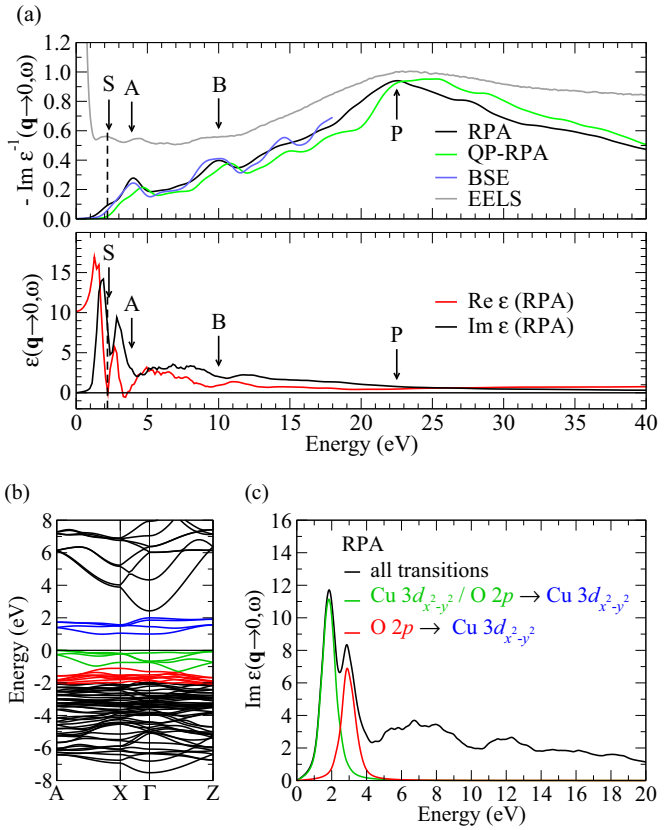

FIG. 2. (a) Direction-averaged loss function $-\operatorname{Im}\varepsilon^{-1}(\mathbf{q}\to 0,\omega)$ in the RPA, with QP corrections (QP-RPA), and QP corrections plus excitonic effects (BSE). Experimental EELS data are given for comparison. The direction-averaged real and imaginary part of the macroscopic dielectric function $\varepsilon(\mathbf{q}\to 0,\omega)$ in the RPA is also displayed. Relevant peak structures are highlighted by arrows and the QP band gap is indicated by a vertical dashed line. (b) Band structure of CuO. (c) Direction-averaged optical absorption spectrum in the RPA. The contributions from relevant interband transitions around the fundamental gap are shown. The involved states are highlighted in the band structure (b) by the corresponding coloring scheme.

weakly (see Fig. 1) which is consistent with their attribution to localized states. For higher $\mathbf{q}$, they lose intensity, whereas a new pronounced excitation at 2.0 eV, which can be assigned to the excitation of a dipole-forbidden d-d exciton [27] above the QP band gap, occurs. Besides this feature, the quality of the RPA description is as good as for simple semiconductors. Since the high-$\mathbf{q}$ d-d excitations do not significantly contribute to the band-gap renormalization (see Sec. IV B), it is justified to rely on the RPA-W as an ingredient for MBPT. Of course this does not mean that RPA works well for all materials and for any required resolution. For instance, multiplet structures in the d-d excitations [27] that are not captured by the RPA could be visible in a loss spectrum. The d-d excitation regime can be well described by considering the local excitonic and multiplet effects as done, e.g., in Ref. [34].

B. Impact of magnetic ordering on the loss function

The IXS and EELS experiments were conducted at room temperature, i.e., in the paramagnetic phase well above the Néel temperatures of 213 and 230 K [6]. All calculations, on the other hand, assume the ground-state antiferromagnetic ordering and a temperature $T = 0$. To estimate the impact of magnetic-ordering-induced temperature effects on the loss function, we calculate and compare the loss spectra for $\mathbf{q}\to 0$ (i.e., the long-range part which dominates the self-energy) for several magnetic structures whose total energies are close to the experimentally observed ground-state magnetic ordering.

TABLE I. Relative total energies E_{tot} per formula unit with respect to the ground-state magnetic ordering AF_{gs}, indirect ($E_{\text{g}}^{\text{ind}}$), and direct ($E_{\text{g}}^{\text{dir}}$) band gaps, and local spin magnetic moments at the Cu (μ_{Cu}) and O (μ_{O}) atoms for various magnetic structures of CuO. All quantities are calculated with the PBE+U functional ($U = 4$ eV).

Ordering	E_{tot} (meV)	$E_{\text{g}}^{\text{ind}}$ (eV)	$E_{\text{g}}^{\text{dir}}$ (eV)	μ_{Cu} (μ_{B})	μ_{O} (μ_{B})
AF_{gs}	0	0.99	1.14	0.55	0.14
$\text{AF}_{[100]}$	19	0.56	0.58	0.55	0.00
$\text{AF}_{[001]}$	29	0.43	0.55	0.54	0.00
$\text{AF}_{[101]}$	87	–	–	0.60	0.02
FM	97	–	–	0.63	0.31

Table I compiles the total energies per formula unit, the indirect and direct band gaps, and the spin magnetic moments at the Cu and O atoms for the ground-state antiferromagnetic ordering AF_{gs}, a ferromagnetic spin arrangement (FM), and the three antiferromagnetic orderings that can be obtained by arranging the spin moments of the Cu ions in the conventional chemical unit cell of CuO [35]. The antiferromagnetic orderings are labeled by the direction of the stacking vector of ferromagnetic Cu planes in the crystal (with respect to the lattice vectors of the conventional chemical unit cell). All orderings have been evaluated within a supercell whose size corresponds to the magnetic unit cell of the AF_{gs} structure.

Thermal fluctuations at room temperature are of the order $k_{\text{B}}T \approx 25$ meV. In terms of their total energies, the orderings AF_{gs}, $\text{AF}_{[100]}$, and $\text{AF}_{[001]}$ have the highest statistical weight in a room-temperature ensemble average among the investigated magnetic structures. These three orderings exhibit a significant band gap already in PBE+U, i.e., without including many-body effects. Figure 3 shows the real and imaginary part of the microscopic dielectric function and the loss function $-\operatorname{Im}\varepsilon^{-1}(\mathbf{q}\to 0,\omega)$ (without crystal local-field effects and quasiparticle lifetimes) for the lowest-energy magnetic orderings AF_{gs}, $\text{AF}_{[100]}$, $\text{AF}_{[001]}$, and $\text{AF}_{[101]}$. In the energy range of optical excitations, the dielectric function for the orderings AF_{gs}, $\text{AF}_{[100]}$, and $\text{AF}_{[001]}$ differs considerably, while the loss function is almost identical. At energies above 5 eV, the dielectric and loss functions of the various magnetic orderings are barely distinguishable. The ordering $\text{AF}_{[101]}$, which does not exhibit a band gap in PBE+U and has a substantially higher total energy (cf. Table I), shows a significantly different optical absorption in the low-energy range, but its loss function is close to the loss functions of the other magnetic orderings. Only the shoulder S, which is a reminiscence of the onset of interband transitions, i.e., the band gap, is obviously not present. Peak A, however, i.e., the plasmonlike low-energy structure, as well as peak B and the main plasmon P are essentially unaffected by the magnetic ordering.

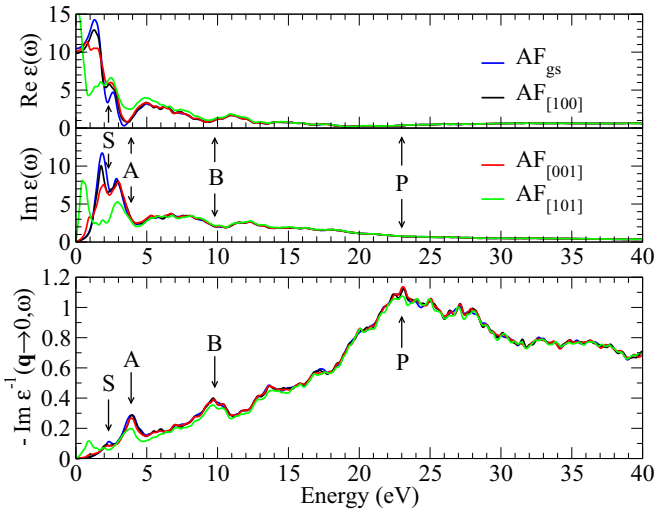

FIG. 3. Impact of the magnetic ordering on the dielectric function and the loss function for $\mathbf{q} \to 0$.

Note also that the magnetic moment of the Cu atoms (see Table I) is rather independent of the long-range magnetic ordering indicating that the local electronic structure is essentially conserved in the paramagnetic phase and only the long-range ordering of the magnetic moments is destroyed. This is in line with experiments that do not observe a strong temperature dependence of spectral features above and below the Néel temperatures apart from a thermal broadening [27]. Based on this analysis, we conclude that the peak structure of the loss function above and below the Néel temperatures does not change noticeably. Thus, measuring at room temperature does not bias the conclusions drawn in our work.

IV. BAND-GAP RENORMALIZATION

Hence we can tackle the *second question*: To which extent does the GWA capture the band-gap renormalization contained in the self-energy? W can be written as an exact multipole expansion

$$W(\omega) = v + \sum_s \frac{2\omega_s W^s}{\omega^2 - \omega_s^2} \tag{1}$$

that contains *all* (charge-fluctuation) excitations s of the system with their excitation energies ω_s and oscillator strengths W^s. They renormalize the bare Hartree-Fock gap that is due to v. Then a diagonal matrix element of the correlation part of the GW self-energy Σ^{GW} evaluated at the QP energy ε_n reads [36]

$$\langle n|\Sigma_C^{GW}(\varepsilon_n)|n\rangle = \sum_i \sum_s \frac{\langle ni|W^s|ni\rangle}{\varepsilon_n - \varepsilon_i - \mathrm{sgn}(\varepsilon_i - \mu)(\omega_s - i\gamma)}, \tag{2}$$

where $\langle ni|W^s|ni\rangle$ are matrix elements in terms of pairs of states, μ is the chemical potential, and γ is a positive infinitesimal to ensure the correct time ordering. Equation (2) shows that the dominant excitations in W lead to peaks in $\mathrm{Im}\,\Sigma(\omega)$. As a consequence, the W corresponding to Fig. 1 entails a rather broad structure in $\mathrm{Im}\,\Sigma(\omega)$ that extends to energies far from the QP gap (see Fig. 4), in contrast to the single plasmon peak in *sp* semiconductors, such as bulk Si which is shown for comparison in Fig. 4. Obviously simple plasmon-pole models are not suitable to describe complex materials like CuO. Still, one might think that solely the strong broad feature in $\mathrm{Im}\,\Sigma(\omega)$ could be enough for the calculation of electron addition and removal spectra. This is, however, not true.

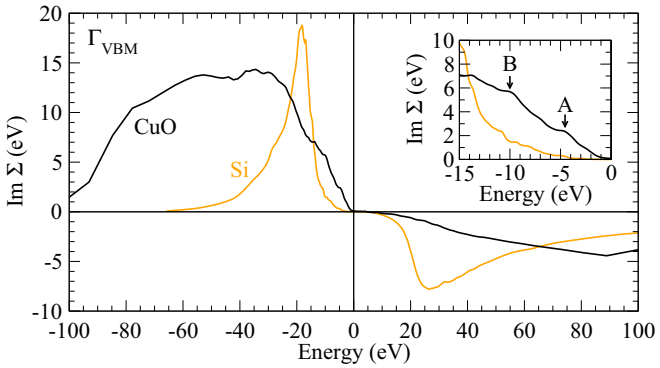

FIG. 4. Comparison of the imaginary part of the self-energy for Si and CuO for the highest valence band at Γ. The respective QP peaks are aligned at zero. In the inset, the peaks in the self-energy that are due to the low-energy plasmonlike excitations in the loss function of CuO are highlighted.

Apart from the broad main structure, the self-energy of CuO exhibits two small peaks at the rising edge (cf. inset of Fig. 4) which are due to the nondispersing peaks A and B in the loss function. Since they add only about 1% to the total spectral weight, one might expect them to be of little importance, although a glance at Eq. (2) tells us to be careful: If one supposes that the main contribution to the self-energy comes from energies around $i = n$, the contribution of each pole is inversely proportional to its energy ω_s. This leads to a significant enhancement of the contributions of the low-energy excitations.

A. Impact of low-energy electronic excitations on the band-gap renormalization

The sensitivity of the peaks in the loss function with respect to changes in the underlying electronic structure can be investigated by applying a scissors shift Δ that rigidly shifts the conduction bands to higher energies. Here we investigate the cases where either all conduction bands ($\Delta = 2$ eV), only the first conduction bands corresponding to the unoccupied Cu $3d_{x^2-y^2}$ states ($\Delta_A = 2$ eV, $\Delta_{\mathrm{rest}} = 0$ eV), or only the remaining conduction bands ($\Delta_A = 0$ eV, $\Delta_{\mathrm{rest}} = 2$ eV) are shifted. In principle, a shift of conduction bands does not have to translate directly into a shift of peaks in the loss function. Figure 5, however, shows that this is sufficiently well fulfilled for the Cu 3*d* states, which is mainly due to the fact that they represent an isolated band complex. Shifting all conduction bands, obviously leads to a blueshift of all loss peaks. If only the unoccupied Cu $3d_{x^2-y^2}$ states are shifted, only peak A is blueshifted in the loss spectrum, while peak B and the main plasmon are not affected. Likewise, a scissors shift affecting all conduction bands but the unoccupied

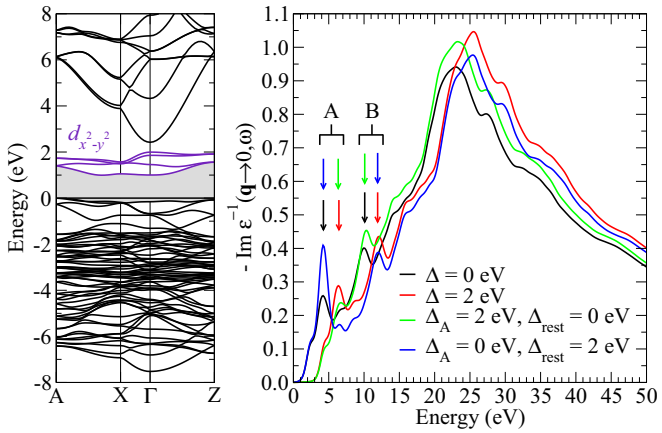

FIG. 5. Shifting the peaks in the loss function by shifting the first conduction-band complex.

Cu $3d_{x^2-y^2}$ states leads to a blueshift of peak B and the main plasmon, whereas peak A does not move. The observed differences in peak intensity are a consequence of the changing real part of the dielectric function.

Table II shows the impact of the shifted peaks in the loss function on the GW results for the Γ-Γ band gap. We recall that a QP self-consistency on G has been performed. Starting from the RPA screening of Fig. 1 yields a band gap of 2.2 eV [15]. As one can see from Table II, blueshifting peak A only ($\Delta_A = 2$ eV) has a much stronger impact on the gap than blueshifting all the remaining spectral weight ($\Delta_{rest} = 2$ eV). Hence, the band-gap renormalization in CuO is to a large extent determined by the low-energy charge excitations. This reminds us of the importance of low-energy excitations for the kinks in the bands of graphene [37], the d bandwidths of correlated metals [38], or the dynamical screening of the effective on-site interaction in La_2CuO_4 [12]. The fact that the GW gap of 2.2 eV is still larger than the observed direct zero-temperature band gap of 1.67 eV [17] may partly be due to the inaccurate description of the low-energy excitations at large $\mathbf{q}$ in the RPA. However, the entire $\mathbf{q}$ range where these peaks appear contributes only about 10%–20% to the total band-gap renormalization as will be shown in the following. Note in particular that in W these features are much smaller than Fig. 1 suggests, since $\mathrm{Im}\,\varepsilon^{-1}(\mathbf{q},\omega) \propto S(\mathbf{q},\omega)/q^2$, i.e., peaks in the DSF contribute with a weight factor $1/q^2$ to the dynamical screening.

B. Contribution of the loss function at large momentum transfers to the band-gap renormalization

Here we estimate how much the screening from different regions in reciprocal space contributes to the renormalization of the fundamental band gap of CuO. We have shown that the calculated loss spectra for low momentum transfers agree well with measured spectra from inelastic x-ray scattering and electron-energy loss (see Fig. 1). However, for large momentum transfers $|\mathbf{q}| > 3$ Å^{-1}, the peak corresponding to the low-energy d-d excitations calculated within the RPA differs from experiment due to the neglect of many-body effects in the calculation. (Nonetheless, the agreement for all other features of the loss function is still excellent, even for the largest momentum transfers.) We have also shown that the low-energy electronic excitations in the loss function play a dominant role in renormalizing the band gap (see Table II). This raises the question whether the discrepancy in the d-d peak position at high momentum transfers may have a significant impact on the gap.

TABLE II. Direct band gap at Γ (in eV) as function of the low-energy excitations in the screening. (See text.)

	$\Delta_A = 0$ eV	$\Delta_A = 2$ eV
$\Delta_{rest} = 0$ eV	2.2	2.8
$\Delta_{rest} = 2$ eV	2.4	3.0

The matrix element of the GW correlation self-energy Σ_C^{GW} at a given QP energy ε_n [cf. Eq. (2)] sums over screening contributions from all vectors $\mathbf{q} = \mathbf{q}_{red} + \mathbf{G}$ in reciprocal space,

$$\langle n|\Sigma_C^{GW}(\varepsilon_n)|n\rangle = \frac{1}{\Omega}\sum_i \sum_s \sum_{\mathbf{q}_{red}\,\mathbf{G}\,\mathbf{G}'} \frac{B_{ni}(\mathbf{q}_{red}+\mathbf{G})B_{ni}^*(\mathbf{q}_{red}+\mathbf{G}')\,W_{\mathbf{G}\mathbf{G}'}^s(\mathbf{q}_{red})}{\varepsilon_n - \varepsilon_i - \mathrm{sgn}(\varepsilon_i-\mu)(\omega_s - i\gamma)}. \quad (3)$$

The excitation energies in W are given by ω_s and the corresponding matrix elements are $W_{\mathbf{G}\mathbf{G}'}^s(\mathbf{q}_{red})$ in reciprocal space [see Eq. (1)]. The sum over s contains discrete excitations and an integral over the continuum. The Bloch integrals that connect orbital to reciprocal space read $B_{ni}(\mathbf{q}_{red}+\mathbf{G}) = \int_\Omega d\mathbf{r}\,\varphi_n^*(\mathbf{r})\,e^{i(\mathbf{q}_{red}+\mathbf{G})\mathbf{r}}\varphi_i(\mathbf{r})$, with $\varphi_n(\mathbf{r})$ a one-particle basis and Ω the crystal volume. The poles of the Green's function are given by ε_i.

In practical calculations, the sum over $\mathbf{q}$ includes only momentum transfers up to a certain cutoff, $|\mathbf{q}| < q_{cut}$, which is linked to the cutoff energy by $E_{cut} = q_{cut}^2/2$. The Γ-Γ band gap E_g of CuO calculated in the GW approximation in first-order perturbation theory (G_0W_0 one-shot approach) is shown as a function of the momentum-transfer cutoff q_{cut} in Fig. 6. The inset of Fig. 6 depicts the relative share of the band-gap renormalization

$$\Delta E_g^{rel}(q_{cut}) = \frac{|E_g(q_{cut}) - E_g(0)|}{|E_g(q_{cut}^{max}) - E_g(0)|} \quad (4)$$

obtained for a certain cutoff q_{cut} with respect to the renormalization for the highly converged value $q_{cut}^{max} = 10$ Å^{-1}. Clearly already 80% to 90% of the band-gap renormalization result from momentum transfers *smaller* than 3 Å^{-1}, i.e., from the range of momentum transfers in the screening where the agreement between theory and experiment is very good also for the low-energy excitations (cf. Fig. 1). Hence, discrepancies between theory and experiment for the high-momentum-transfer–low-energy excitations have only minor impact on the band gap renormalization.

V. SUMMARY AND CONCLUSIONS

In summary, by combining state-of-the-art IXS experiments with *ab initio* calculations, we have shown that the RPA screening captures the most important electronic excitations

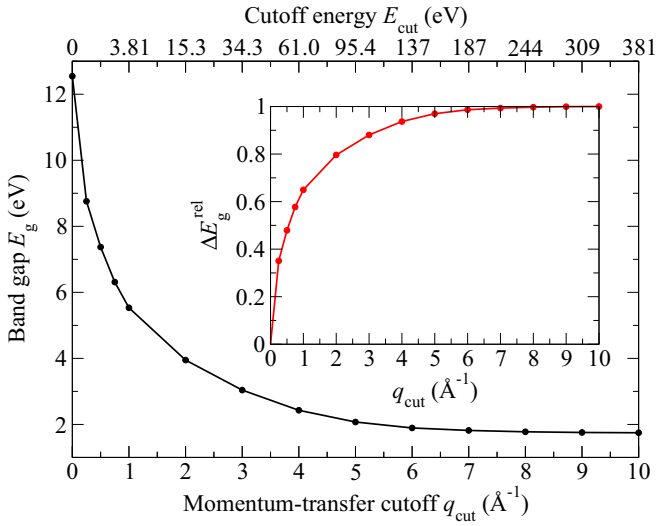

FIG. 6. One-shot G_0W_0 band gap of CuO including screening contributions up to a momentum transfer q_{cut}. The inset shows the relative share of band-gap renormalization ΔE_g^{rel} obtained when screening contributions up to a cutoff q_{cut} are taken into account.

occurring in the measurable loss function of CuO with great accuracy. This experimentally verified screening allows us to demonstrate that the band-gap renormalization in CuO is strongly influenced by low-energy charge excitations.

The fact that RPA yields excellent loss spectra except for *d*-*d* excitations at high **q** is of wider interest: In the context of methods that treat correlations explicitly (such as DMFT), the screening of the on-site interaction U can be calculated from first principles in the constrained RPA [39]. In this approach, the low-energy excitations are excluded from the RPA calculation, since they are implicitly taken into account in the DMFT cycle. The mutual cancellations of quasiparticle corrections and excitonic effects shown in Fig. 2 illustrate why the constrained RPA is sufficiently precise to determine the screened on-site interaction.

Our findings suggest the following picture for MBPT in CuO: (i) The RPA captures many features of W because self-energy corrections and vertex corrections in W cancel to a large extent for the main plasmon (like in simple semiconductors) and for the localized low-energy excitations (similar to excitations in a one-electron system [30]). Note that the RPA depends on the density functional used for the ground-state calculation [40]. Thus, a good description of the ground-state density is indispensable. (ii) This explains why QP self-consistent calculations using a GW-RPA W require a downscaling of W by an empirical factor of about 0.8 [41]. (iii) At large **q**, the cancellation is less effective leading to a residual error of the RPA. The final GW band-gap renormalization is, however, not very sensitive to this, since the QP energies around the gap are dominated by excitations at *small* **q**. (iv) All GW calculations neglect the vertex Γ in the expression $\Sigma = iGW\Gamma$ for the self-energy. Our results suggest that the contribution of this correction may be visible, but not vital to understand the band-gap renormalization in CuO. Note that this does not have to hold for other features such as the satellites in the one-particle spectral function [42,43].

In conclusion, it is of paramount importance for GW calculations of systems with low-energy transitions between localized states that the screened Coulomb interaction W features all relevant excitations occurring in the *measurable* loss spectrum at low and medium momentum transfers. Our approach of dissecting many-body theory into its measurable ingredients represents a generalizable ansatz to better understand MBPT for complex systems in a joint effort of theory and experiment and promises to be useful for future theoretical developments.

ACKNOWLEDGMENTS

Financial support has been provided by the European Commission Marie Curie Actions within the framework of the CEA Eurotalents program, the European Research Council under the EU FP7 framework program (ERC Grant No. 320971), and the Academy of Finland (Grants No. 1259526, No. 1260204, No. 1283136, No. 1254065). This work has benefited from collaboration with the Maison de la Simulation. Computer time has been granted by GENCI (project 544). We gratefully acknowledge the ESRF for provision of beamtime.

[1] G. A. Sawatzky, Nature (London) **342**, 480 (1989).
[2] N. F. Mott, Proc. Phys. Soc. A **62**, 416 (1949).
[3] J. Hubbard, Proc. R. Soc. London Ser. A **276**, 238 (1963).
[4] A. Georges, G. Kotliar, W. Krauth, and M. J. Rozenberg, Rev. Mod. Phys. **68**, 13 (1996); G. Kotliar, S. Y. Savrasov, K. Haule, V. S. Oudovenko, O. Parcollet, and C. A. Marianetti, *ibid.* **78**, 865 (2006).
[5] M. S. Hybertsen and S. G. Louie, Phys. Rev. B **34**, 5390 (1986); R. W. Godby and R. J. Needs, Phys. Rev. Lett. **62**, 1169 (1989).
[6] J. B. Forsyth, P. J. Brown, and B. M. Wanklyn, J. Phys. C **21**, 2917 (1988); B. X. Yang, T. R. Thurston, J. M. Tranquada, and G. Shirane, Phys. Rev. B **39**, 4343 (1989).
[7] T. Kimura, Y. Sekio, H. Nakamura, T. Siegrist, and A. P. Ramirez, Nat. Mater. **7**, 291 (2008).
[8] J. G. Bednorz and K. A. Müller, Z. Phys. B **64**, 189 (1986).
[9] W. Y. Ching, Y.-N. Xu, and K. W. Wong, Phys. Rev. B **40**, 7684 (1989); A. Svane and O. Gunnarsson, Phys. Rev. Lett. **65**, 1148 (1990); Z. Szotek, W. M. Temmerman, and H. Winter, Phys. Rev. B **47**, 4029 (1993); A. Filippetti and V. Fiorentini, Phys. Rev. Lett. **95**, 086405 (2005); D. Wu, Q. Zhang, and M. Tao, Phys. Rev. B **73**, 235206 (2006); X. Rocquefelte, M.-H. Whangbo, A. Villesuzanne, S. Jobic, F. Tran, K. Schwarz, and P. Blaha, J. Phys.: Condens. Matter **22**, 045502 (2010); M. Heinemann, B. Eifert, and C. Heiliger, Phys. Rev. B **87**, 115111 (2013).
[10] F. C. Zhang and T. M. Rice, Phys. Rev. B **37**, 3759 (1988); H. Eskes, L. H. Tjeng, and G. A. Sawatzky, *ibid.* **41**, 288 (1990).
[11] A. I. Lichtenstein and M. I. Katsnelson, Phys. Rev. B **62**, R9283 (2000); N. Lin, E. Gull, and A. J. Millis, *ibid.* **80**, 161105 (2009); C. Weber, K. Haule, and G. Kotliar, Nat. Phys. **6**, 574 (2010);

M. Ferrero, O. Parcollet, A. Georges, G. Kotliar, and D. N. Basov, Phys. Rev. B **82**, 054502 (2010); T. Ahmed, J. J. Kas, and J. J. Rehr, *ibid.* **85**, 165123 (2012).

[12] P. Werner, R. Sakuma, F. Nilsson, and F. Aryasetiawan, Phys. Rev. B **91**, 125142 (2015).

[13] S. V. Faleev, M. van Schilfgaarde, and T. Kotani, Phys. Rev. Lett. **93**, 126406 (2004); C. Rödl, F. Fuchs, J. Furthmüller, and F. Bechstedt, Phys. Rev. B **77**, 184408 (2008); **79**, 235114 (2009); H. Jiang, R. I. Gomez-Abal, P. Rinke, and M. Scheffler, *ibid.* **82**, 045108 (2010).

[14] S. Lany, Phys. Rev. B **87**, 085112 (2013).

[15] C. Rödl, F. Sottile, and L. Reining, Phys. Rev. B **91**, 045102 (2015).

[16] L. Hedin, Phys. Rev. **139**, A796 (1965).

[17] F. Marabelli, G. B. Parravicini, and F. Salghetti-Drioli, Phys. Rev. B **52**, 1433 (1995).

[18] F. Polack, M. Silly, C. Chauvet, B. Lagarde, N. Bergeard, M. Izquierdo, O. Chubar, D. Krizmancic, M. Ribbens, J.-P. Duval, C. Basset, S. Kubsky, and F. Sirotti, AIP Conf. Proc. **1234**, 185 (2010).

[19] M. Zurkirch, M. DeCrescenzi, M. Erbudak, and A. R. Kortan, Phys. Rev. B **56**, 10651 (1997).

[20] G. Kresse and J. Furthmüller, Comput. Mater. Sci. **6**, 15 (1996); G. Kresse and D. Joubert, Phys. Rev. B **59**, 1758 (1999).

[21] M. Shishkin and G. Kresse, Phys. Rev. B **74**, 035101 (2006); M. Shishkin, M. Marsman, and G. Kresse, Phys. Rev. Lett. **99**, 246403 (2007).

[22] S. Åsbrink and L.-J. Norrby, Acta Crystallogr. B **26**, 8 (1970).

[23] The lattice vectors $\{\mathbf{a}',\mathbf{b}',\mathbf{c}'\}$ of the primitive magnetic unit cell for the ground-state antiferromagnetic ordering used in the calculations are related to the lattice vectors $\{\mathbf{a},\mathbf{b},\mathbf{c}\}$ of the conventional chemical unit cell by $\mathbf{a}' = \mathbf{a} + \mathbf{c}$, $\mathbf{b}' = \mathbf{b}$, and $\mathbf{c}' = -\mathbf{a} + \mathbf{c}$.

[24] J. P. Perdew, K. Burke, and M. Ernzerhof, Phys. Rev. Lett. **77**, 3865 (1996).

[25] W. Hanke and L. J. Sham, Phys. Rev. B **21**, 4656 (1980); G. Strinati, Riv. Nuovo Cimento **11**, 1 (1988); M. Rohlfing and S. G. Louie, Phys. Rev. B **62**, 4927 (2000); G. Onida, L. Reining, and A. Rubio, Rev. Mod. Phys. **74**, 601 (2002).

[26] H. Hayashi, Y. Udagawa, W. A. Caliebe, and C.-C. Kao, Phys. Rev. B **66**, 033105 (2002); G. Döring, C. Sternemann, A. Kaprolat, A. Mattila, K. Hämäläinen, and W. Schülke, *ibid.* **70**, 085115 (2004); G. Ghiringhelli, A. Piazzalunga, X. Wang, A. Bendounan, H. Berger, F. Bottegoni, N. Christensen, C. Dallera, M. Grioni, J.-C. Grivel, M. Moretti Sala, L. Patthey, J. Schlappa, T. Schmitt, V. Strocov, and L. Braicovich, Eur. Phys. J. Spec. Top. **169**, 199 (2009).

[27] W. B. Wu, N. Hiraoka, D. J. Huang, S. W. Huang, K. D. Tsuei, M. van Veenendaal, J. van den Brink, Y. Sekio, and T. Kimura, Phys. Rev. B **88**, 205129 (2013); S. Huotari, L. Simonelli, C. J. Sahle, M. Moretti Sala, R. Verbeni, and G. Monaco, J. Phys.: Condens. Matter **26**, 165501 (2014).

[28] E. A. Bakulin, M. M. Bredov, E. G. Ostroumova, and V. V. Shcherbinina, Fiz. Tverd. Tela (Leningrad) **19**, 1307 (1977) [Sov. Phys. Solid State **19**, 760 (1977)].

[29] V. Olevano and L. Reining, Phys. Rev. Lett. **86**, 5962 (2001).

[30] F. Iori, F. Rodolakis, M. Gatti, L. Reining, M. Upton, Y. Shvyd'ko, J.-P. Rueff, and M. Marsi, Phys. Rev. B **86**, 205132 (2012).

[31] N. Vast, L. Reining, V. Olevano, P. Schattschneider, and B. Jouffrey, Phys. Rev. Lett. **88**, 037601 (2002).

[32] K. Sturm, W. Schülke, and J. R. Schmitz, Phys. Rev. Lett. **68**, 228 (1992).

[33] C. Rödl and F. Bechstedt, Phys. Rev. B **86**, 235122 (2012); C. Guedj, L. Hung, A. Zobelli, P. Blaise, F. Sottile, and V. Olevano, Appl. Phys. Lett. **105**, 222904 (2014).

[34] M. W. Haverkort, M. Zwierzycki, and O. K. Andersen, Phys. Rev. B **85**, 165113 (2012).

[35] Note that the primitive unit cell that describes the ground state ordering AF_{gs} is twice as big as the conventional chemical unit cell.

[36] L. Hedin, J. Phys.: Condens. Matter **11**, R489 (1999).

[37] P. E. Trevisanutto, C. Giorgetti, L. Reining, M. Ladisa, and V. Olevano, Phys. Rev. Lett. **101**, 226405 (2008).

[38] M. Gatti and M. Guzzo, Phys. Rev. B **87**, 155147 (2013).

[39] F. Aryasetiawan, M. Imada, A. Georges, G. Kotliar, S. Biermann, and A. I. Lichtenstein, Phys. Rev. B **70**, 195104 (2004).

[40] A. G. Eguiluz, O. D. Restrepo, B. C. Larson, J. Z. Tischler, P. Zschack, and G. E. Jellison, J. Phys. Chem. Solids **66**, 2281 (2005).

[41] A. N. Chantis, M. van Schilfgaarde, and T. Kotani, Phys. Rev. B **76**, 165126 (2007).

[42] J. Ghijsen, L. H. Tjeng, J. van Elp, H. Eskes, J. Westerink, G. A. Sawatzky, and M. T. Czyzyk, Phys. Rev. B **38**, 11322 (1988).

[43] Z.-X. Shen, R. S. List, D. S. Dessau, F. Parmigiani, A. J. Arko, R. Bartlett, B. O. Wells, I. Lindau, and W. E. Spicer, Phys. Rev. B **42**, 8081 (1990).